Bioceramic Nanocomposite Thiol-Acrylate PolyHIPE Scaffolds for Enhanced Osteoblastic Cell Culture in 3D

Aaron Lee[a], Caitlin R. Langford[a], Luis M. Rodriguez-Lorenzo[b,c], Helmut Thissen*[d], Neil R. Cameron*[a,e]

[a] Department of Materials Science and Engineering, Monash University, 22 Alliance Lane, Clayton, VIC 3800, Australia

[b] Institute of Polymer Science and Technology, ICTP-CSIC, Juan de la Cierva 3, 28006-Madrid, Spain

[c] Networking Biomedical Research Centre in Bioengineering, Biomaterials and Nanomedicine, CIBER-BBN, Spain

[d] CSIRO Manufacturing, Bayview Avenue, Clayton VIC 3168, Australia

[e] School of Engineering, University of Warwick, Coventry CV4 7AL, U.K.

Corresponding authors**:** neil.cameron@monash.edu; helmut.thissen@csiro.au

Abstract

Emulsion-templated (polyHIPE) scaffolds for bone tissue engineering were produced by photopolymerisation of a mixture of trimethylolpropane tris(3-mercaptopropionate) and dipentaerythritol penta-/hexa-acrylate in the presence of hydroxyapatite (HA) or strontium-modified hydroxyapatite (SrHA) nanoparticles. Porous and permeable polyHIPE materials were produced regardless of the type or incorporation level of the bioceramic, although higher loadings resulted in a larger average pore diameter. Inclusion of HA and SrHA into the scaffolds was confirmed by EDX-SEM, FTIR and XPS and quantified by thermogravimetry. Addition of HA to polyHIPE scaffolds significantly enhanced compressive strength (148-216 kPa) without affecting compressive modulus (2.34-2.58 MPa). The resulting materials were evaluated *in vitro* as scaffolds for the 3D culture of MG63 osteoblastic cells vs a commercial 3D cell culture scaffold (Alvetex®). Cells were able to migrate throughout all scaffolds, achieving a high density by the end of the culture period (21 days). The presence of HA and in particular SrHA gave greatly enhanced cell proliferation, as determined by staining of histological sections and total protein assay (Bradford). Furthermore, Von Kossa and Alizarin Red staining demonstrated significant mineralisation from inclusion of bioceramics, even at the earliest time point (day 7). Production of alkaline phosphatase (ALP), an early osteogenic marker, was used to investigate the influence of HA and SrHA on cell function. ALP levels were significantly reduced on HA- and SrHA-modified scaffolds by day 7, which agrees with the observed early onset of mineralisation in the presence of the bioceramics. The presented data support our conclusions that HA and SrHA enhance osteoblastic cell

proliferation on polyHIPE scaffolds and promote early mineralisation.

Introduction

The generation of fully functional and vascularized bone tissue suitable for application in both load bearing and non-load bearing situations remains an unmet challenge in tissue engineering. Progress requires a complex integration of a number of factors, including, but not limited to: a scaffold with appropriate morphology, physical and mechanical properties, together with degradation rate, to permit integration of the neo-tissue *in vivo*; chemical and/or biological factors to promote osteogenesis; and a hierarchy of pore sizes that promotes both vascularization and neo-bone formation[1]. Many scaffold materials and fabrication technologies have been explored, including supercritical foaming of carbon dioxide, 3D printing of materials, particle templating, thermally induced phase separation (TIPS) and electrospinning[2-5]. No single scaffold type has emerged as a generic substrate for the successful engineering of vascularized bone tissue. Amongst the problems associated with traditional methods of scaffold production are: poor interconnectivity (hard-sphere templating); irregular and poorly defined morphology (TIPS scaffolds); limited cell penetration (electrospun scaffolds); lack of scaleabililty (scaffolds by 3D printing).

Highly porous polymers with a well-defined and fully interconnected porosity can be prepared readily by a templating process involving a high internal phase emulsion (HIPE)[6-17]. The HIPE is created with a droplet volume fraction of at least 74%[18], after which the continuous (non-droplet) phase is solidified to create a monolithic, porous material. The resulting materials, known as polyHIPEs, have found application in diverse areas of technology, including separation/filtration, solid phase synthesis, heterogeneous catalysis

and gas storage[19-26]. In recent years, polyHIPEs have undergone intense investigation as scaffolds for cell culture and tissue engineering[27-49]. Non-degradable styrenic polyHIPE materials have been shown to provide a suitable environment for the *in vitro* culture of a wide variety of cell types in 3D[28, 30-33, 35, 38, 39]. These scaffolds are available commercially under the tradename Alvetex®. In our group, we have devoted recent efforts to the generation of degradable polyHIPE scaffolds for regenerative applications. This can be achieved by the photochemically-induced step-growth polymerisation of multifunctional thiols and alkenes or alkynes. In particular, commercially available multifunctional acrylates are convenient comonomers for this process[37, 50-52]. The resulting degradable porous scaffolds have been shown to be suitable substrates for the 3D culture of keratinocytes[37] and fibroblasts[51]. These previous studies demonstrated the biocompatibility of these scaffolds using two different cell types and, importantly, also showed that the scaffold degradation products did not compromise cell viability. Significant cell attachment and infiltration into the scaffolds was demonstrated up to 11 days in culture.

Hydroxyapatites have been described as bioactive materials that directly regulate the behaviour of both normal and transformed cells. In particular, osteoblasts show enhanced maturation and functional activity in the presence of hydroxyapatite[53]. Strontium-containing hydroxyapatites support increased osteoblast adhesion, proliferation and viability in culture when compared with calcium hydroxyapatites. The dissolution products, apparently strontium (Sr^{2+}) from Sr-coated implants, have been found to enhance the alkaline phosphatase (ALP) activity and *in vitro* mineralization ability of MSC cells[40]. Strontium was

also found to have antiresorptive and anabolic activities and has been thought to have potential interest for the treatment of osteoporosis. More recently, Sr^{2+} has been shown to promote angiogenic expression and to modify the net positive charge on calcium phosphate nanoparticles[54].

In this article, we describe the preparation of degradable thiol-acrylate polyHIPE scaffolds (Figure 1) loaded with inorganic nanoparticles as a substrate for the culture of osteoblastic cells in 3D. Two types of nanoparticle were used: commercially available hydroxyapatite (HA); and in-house prepared strontium-substituted HA (SrHA). The resulting materials were subjected to thorough physical, chemical and mechanical analysis, and were subsequently used for the culture of osteoblastic cells (MG63) in 3D. We note previous work on the use of hydroxyapatite-modified non-degradable polystyrene polyHIPE materials for osteoblastic cell culture[27].
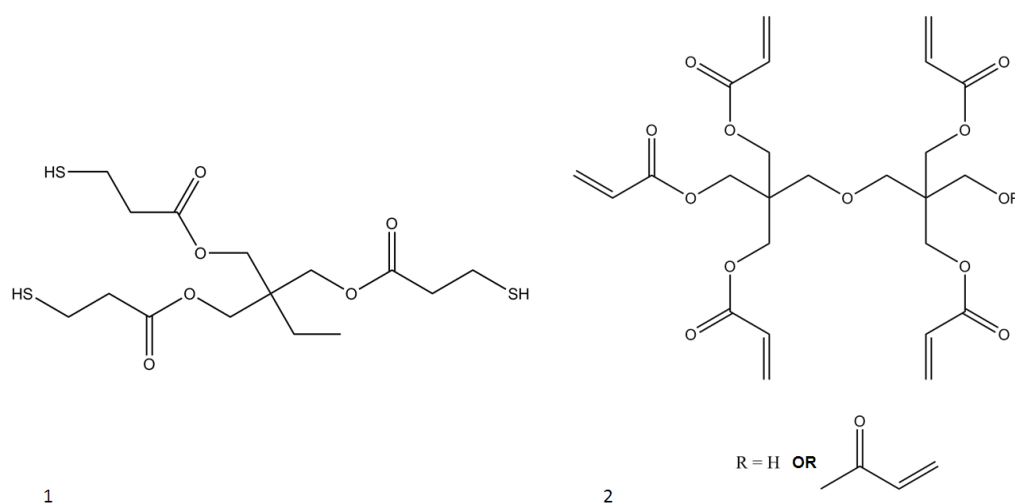

Figure 1. Monomers used to prepare the polyHIPE scaffolds by UV-initiated thiol-ene click

chemistry. Monomer 1 is trimethylolpropane tris(3-mercaptopropionate), monomer 2 is dipentaerythritol penta-/hexa-acrylate.

Materials and Methods

Materials

Trimethylolpropane tris(3-mercaptopropionate) (TMPTMP), dipentaerythritol penta-/hexa-acrylate (DPEHA), 1,2-dichloroethane, dichloromethane, diphenyl (2, 4, 6-trimethylbenzoyl) phosphine oxide/2-hydroxy-2-methylpropiophenone blend, Pluronic F108, strontium hexachloride, nitric acid and hydroxyapatite were purchased from Sigma-Aldrich and used without modification. Hypermer B246 was obtained from Croda while Alvetex® 3D scaffolds were purchased from Reinnervate Ltd. Complete media for culture experiments was formulated using Dulbecco's Modified Eagle Medium 11995-065 with 10% foetal bovine serum and 1% penicillin/streptomycin purchased from Life Technologies through Thermo Fisher Scientific. Alkaline phosphatase (ALP) activity was determined using an ALP assay kit (Abcam).

Preparation of Strontium-substituted hydroxyapatite

Strontium chloride solution was dissolved in 250 mL of deionised water to a concentration of 10^{-3}M and pH adjusted to 7.24. Strontium-substitution was achieved by adding 0.5 g hydroxyapatite per 50 mL of strontium chloride solution agitated on an orbital shaker for

three hours. The solutions were then centrifuged at 3000 rpm for three minutes with the supernatant collected for inductively coupled plasma optical emission spectrometry (ICP-OES) analysis. The pellet itself was subsequently frozen and freeze-dried over two days. Post-sorption supernatant and the original strontium chloride solution were acidified and diluted with 2% HNO_3 and analysed using a Varian 730-ES axial ICP-OES. Certified multi-element solutions were used to check the accuracy of the calibration standards used. Powders were also analysed by X-ray diffraction (XRD) with a Bruker D8 Advance X-ray diffractometer operating under CuKα radiation (40 kV, 40 mA) and equipped with a LynxEye detector. Samples were scanned between 3.5°<2θ<130° with a step size of 0.02° and a count time of 1.6 seconds per step. Analyses were performed using the Bruker XRD search match program EVA[TM] with crystalline phases identified using the ICCD-JCPDS powder diffraction database. Rietveld analyses were performed using the Bruker TOPAS [TM] V5 program to determine the lattice parameters.

Preparation of PolyHIPEs

The oil phase of the emulsion was prepared by initially dissolving the surfactant Hypermer B246 (0.46 g) in 7.0mL of 1, 2-dichloroethane. TMPTMP (4.84 g) and DPEHA (3.47 g) are subsequently added and mixed well to create the monomer mixture (total volume 14 mL). The monomer mixture is then transferred to a multi-necked flask and 0.7 mL of photoinitiator (diphenyl (2, 4, 6-trimethylbenzoyl) phosphine oxide/2-hydroxy-2-methylpropiophenone blend) was added. Water was added dropwise while an overhead

8

stirrer attached to a D-paddle emulsified the mixture at 300 rpm. The emulsion was homogenised for 5 minutes from the addition of water and poured into a cylindrical polytetrafluoroethylene mould with an internal diameter of 27 mm and a height of 25 mm which was then sandwiched between two glass plates. The mould was then transferred to a conveyor belt travelling at 3.2 m/s and passed under a Heraeus Fusion Systems UV lamp to initiate photopolymerisation. The sample was passed under the lamp four times (two on each side) with a power output of 5.7 W/cm^2 per run. Polymerised samples were removed from their moulds and transferred to an acetone bath and subsequently washed in a soxhlet with dichloromethane over 24 hours to remove any residual organic components.

Incorporation of hydroxyapatites into the scaffolds was achieved by dispersing the ceramic through the monomer phase prior to emulsification with formulations outlined in Table 1. Emulsification and polymerisation were carried out immediately to minimise sedimentation and agglomeration. Samples were then washed in acetone and dichloromethane in a Soxhlet for 24h each, then dried at room temperature under atmospheric pressure.

Table 1. Formulations of polyHIPE scaffolds containing hydroxyapatite (HA) and strontium-substituted hydroxyapatite (SrHA).

Sample[a]	HA(g)	SrHA (g)	Pluronic F108 (mg)
PHP-5HA	0.7	-	7

PHP-5SrHA	-	0.7	7
PHP-10HA	1.4	-	14

[a] PHP: High internal phase emulsion templated polymers prepared using TMPTMP and DPEHA as co-monomers, PHP-5HA: hydroxyapatite loading of 5 wt% relative to volume of the monomer mixture, PHP-5SrHA: strontium substituted hydroxyapatite loading of 5 wt% relative to volume of the monomer mixture, PHP-10HA: hydroxyapatite loading of 10 wt% relative to volume of the monomer mixture.

Scanning electron microscopy

PolyHIPE morphology was determined by imaging cut samples using a FEI Nova NanoSEM 450 FEGSEM operating at 5 kV. Samples of fractured polyHIPE were mounted on aluminium stubs fitted with adhesive carbon fibre pads with the fractured surface face up. Samples were coated with iridium using a Cressington 208 HR sputter coater. Images were then analysed using ImageJ and a void size estimate was determined by measuring the diameters of 100 randomly chosen voids. To account for random sectioning of voids a statistical correction factor of $2/3^{1/2}$ was employed to improve the accuracy of the result[55, 56]. Energy-dispersive X-ray spectroscopy (EDX) analysis of incorporated hydroxyapatite was performed using a Bruker Quantax 400 x-ray system.

FTIR Spectroscopy

FTIR spectroscopy was used to identify compositional differences between the native

fabricated polyHIPE and the composite. Samples were pressed onto the sensor for a Thermo Scientific ATR FTIR Nicolet 6700 system and scanned 16 times with a resolution of 4 cm^{-1}.

X-ray photoelectron spectroscopy (XPS)

X-ray photoelectron spectroscopy (XPS) analysis was performed using an AXIS Nova spectrometer (Kratos Analytical Inc., Manchester, UK) with a monochromated Al K$_\alpha$ source at a power of 150 W (15 kV × 10 mA) and a hemispherical analyser operating in the fixed analyser transmission mode. The total pressure in the main vacuum chamber during analysis was typically between 10^{-9} and 10^{-8} mbar. Survey spectra were acquired at a pass energy of 160 eV. To obtain more detailed information about chemical structure, oxidation states etc., high resolution spectra were recorded from individual peaks at 40 eV pass energy (yielding a typical peak width for polymers of 1.0 eV). Each specimen was analysed at an emission angle of 0° as measured from the surface normal. Assuming typical values for the electron attenuation length of relevant photoelectrons the XPS analysis depth (from which 95 % of the detected signal originates) ranges between 5 and 10 nm for a flat surface. As the actual emission angle is ill-defined for rough surfaces and powders (ranging from 0º to 90º), the sampling depth may range from 0 nm to approximately 10 nm. Data processing was performed using CasaXPS processing software version 2.3.15 (Casa Software Ltd., Teignmouth, UK). All elements present were identified from survey spectra. The atomic concentrations of the detected elements were calculated using integral peak intensities and the sensitivity factors supplied by the manufacturer.

Thermogravimetric Analysis

Thermogravimetric analysis was performed on composite materials in order to determine the level of ceramic content loaded. Samples were loaded onto an alumina sample holder and analysed using the Netzsch STA 449 F1 Jupiter Simultaneous TGA/DSC Thermal Analyser system. A temperature ramp rate of 10 °C/min was applied to a maximum temperature of 900 °C to facilitate polymer burn off. Chamber conditions were controlled by flowing nitrogen through at a rate of 40 mL/min. Measurements were carried out using a Type S DSC sensor. Mass loss for each sample was then determined as a percentage and averaged across three trials.

Scaffold Preparation

Scaffolds used for culture of MG63 cells were prepared by cutting polymerised monoliths with a Leica VT1000S vibrating microtome at a thickness of 200 μm. A 15 mm bore was used to excise circular scaffold samples for *in vitro* culture. Samples were then dipped in ethanol and water and dried on filter paper to flatten. PolyHIPE scaffold discs were then mounted in well inserts in a biosafety hood and placed into a 6-well plate. Sterilisation of scaffolds was performed by washing in 80% ethanol thrice for 15 minutes.

Compression Testing

Cylindrical scaffold sections with a diameter of 5 mm and a height of 2 mm were subjected to uniaxial compression in an Instron 5500R with a 10 N load cell. A cross head speed of 0.25 mm/min was applied until 12.5% sample deformation had been achieved. Data was collected using BlueHill3 software version 3.3 and analysed in MATLAB. The linear region of the load-deflection curve was fitted with a regression curve (R^2>0.99) and used to calculate the strain of deformation. Load at 10% specimen deformation or the yield point (whichever was lower) was then used to calculate the strength. Compressive strength was determined by dividing the load by the initial cross-sectional area of the sample. The compressive modulus was determined by reading the load and deformation at the steepest straight line portion of the curve and evaluating using Equation [1].

$$E_C = \frac{WH}{AD} \hspace{4cm} [1]$$

where, E_c is the modulus of elasticity in compression (Pa), W is the load (N), A is the initial cross-sectional area (m^2) and D is the deformation (m). Statistical differences were determined by applying a one-way ANOVA with the Holm-Sidak approach in comparing the difference in sample means.

Cell Culture and histology

Scaffolds were pre-treated by washing in ethanol followed by phosphate buffered saline and complete media and allowed to incubate overnight at 37 °C, 5% pCO$_2$. Media was then replaced to half of the total culture volume (5mL). MG63 osteosarcoma cells (ATCC) were seeded at a density of 0.5x10^6 cells per scaffold to the scaffold surface and incubated overnight to allow for cell attachment. Media was then topped up to 10 mL and maintained for the remainder of the culture period with a replacement every 2-3 days. Scaffolds were then harvested at days 7, 14 and 21 for fixing with formalin and embedding in paraffin wax processed using the Leica Peloris rapid tissue processor. Cross-sections 10μm thick were mounted on slides and stained. Processing for von Kossa's (VK) involved bringing paraffin sections to water and placed in 1.5% silver nitrate solution and left in strong light for one hour. Slides were then washed in water and counterstained with nuclear fast red for ten minutes. Additional slides in paraffin were placed in 0.5% Alizarin Red S (AR) solution for one hour and rinsed in 1% sodium hydroxide for 5 seconds. Slides were then dehydrated in absolute ethanol, cleared in xylene and mounted. Slides were imaged using a Nikon Eclipse TS100 microscope in bright-field and captured using Q-Capture Pro 7.

Bradford Assay

Scaffolds were removed from their inserts, washed three times in cold, sterile PBS, and cut into small (~ 1 mm) pieces with sterile scissors. The scaffold pieces were placed in a pre-

cooled Eppendorf tube, and 500 μl radioimmunoprecipitation assay (RIPA) buffer containing 5 μl protease cocktail inhibitor added. The scaffolds were then incubated on ice for 15 minutes, with vortexing every 3 minutes for 30 seconds in order to dislodge the cells from the scaffold. Samples were then centrifuged at 12,000 rpm for 15 minutes at 4 ^{o}C in order to pellet the scaffold and cell debris. The supernatant was then removed, placed in a fresh pre-cooled Eppendorf tube, and diluted 1:40 in PBS.

A bovine serum albumin (BSA) protein ladder was prepared in order to give 9 standards ranging in concentration from 2 mgml^{-1} to 0 mgml^{-1}. 10 μl of each sample or standard was pipetted into a flat-bottom 96 well plate. 300 μl Coomassie Plus Reagent was then added to each well and mixed thoroughly. The plate was then incubated for 10 minutes at room temperature, and the absorbance read at 595 nm using a Thermo Scientific Multiskan Spectrum plate reader. The Bradford assay was performed in triplicate for each material and culture time tested. The mean and standard deviation were determined and a two-way analysis of variance (ANOVA). A Tukey post-hoc test for multiple comparisons was performed with $p < 0.05$ to determine statistical differences.

Alkaline Phosphatase (ALP) Assay

Scaffolds were prepared for ALP assay using the same method as described above for Bradford assay, with ALP assay buffer replacing RIPA buffer. The obtained supernatant was collected and placed in a fresh pre-cooled Eppendorf tube.

120 µl standard solutions of *para*-nitrophenylphosphate (*p*NPP), with concentrations ranging from 0 nmol well^{-1} to 20 nmol well^{-1}, were added to 2 wells of a 96 well plate, and 80 µl of each samples added to a further 3 wells. 50 µl of a 5 mM *p*NPP solutions was then added to each sample well, followed by the addition of 10 µl ALP enzyme to each standard well. The plate was then protected from light, and incubated at 25 ^{o}C for 1 hour. 10 µl stop solution was then added to each well, and the absorbance measured at 405 nm using a Thermo Scientific Multiskan Spectrum plate reader. The Bradford assay was performed in triplicate for each material and culture time tested. Mean and standard deviation were determined, a two-way ANOVA and Tukey post-hoc test were applied to determine statistical significance.

Results

Strontium substitution into hydroxyapatite

Hydroxyapatite was added to a solution of strontium chloride and agitated to facilitate adsorption and ion exchange. ICP-OES and XRD were used to evaluate the incorporation of strontium. Ion concentrations of Sr^{2+} and Ca^{2+} were compared between the original strontium chloride solution and the post-sorption supernatant. Approximately 40% of the strontium initially present in solution is removed with the hydroxyapatite.

Table 2. ICP-OES and XRD analysis of Sr-modified hydroxyapatite nanoparticles

16

	ICP-OES (mM)			Lattice Parameters (A)	
Sample	Sr	Ca	Powder Sample	a	c
Strontium Chloride solution	0.90	3.0×10^{-3}	HA	9.424±0.001	6.883±0.001
Supernatant	0.53	0.96	Sr-HA	9.429±0.001	6.890±0.001

XRD patterns of the original hydroxyapatite powder sample and the post-sorption hydroxyapatite were obtained and a Rietveld refinement applied (Figure S1). Lattice parameters obtained in the post-sorption sample are larger than the unaltered hydroxyapatite by more than three standard deviations. This indicates that it is probable that strontium has been incorporated through substitution into the hydroxyapatite lattice structure.

Morphology of polyHIPE scaffolds

PolyHIPE scaffolds with a nominal porosity of 90% were prepared using the monomers TMPTMP and DPEHA. Hydroxyapatite and Sr-modified hydroxyapatite nanoparticles were incorporated by mechanical dispersion through the monomer phase prior to emulsification and curing. A homogeneous distribution of particles was obtained by stirring the solution with a magnetic stirrer at 500 rpm for one hour. The amount of hydroxyapatite added to each sample was determined as a function of the total monomer volume (14 mL) and

partially stabilised with Pluronic F108. Hydroxyapatite incorporation into the polyHIPE scaffold was evaluated as a function of concentration between 0-10% with representative areas depicted in Figure 2. Morphological features which hallmark polyHIPE materials such as rounded interior and highly interconnected pores are evident in all materials. As the concentration of hydroxyapatite in the formulation is increased, the ceramic becomes visible on the scaffold interior and covers an increasing area of the available surface. From Figure 2, there is very little difference in the morphology of the scaffolds produced with 0 wt% hydroxyapatite and those with 5 wt% hydroxyapatite. At higher concentrations, there appears to be a marked destabilising effect leading to extremely large internal voids. Detailed characterisation of morphology and porosity of the parent (hydroxyapatite-free) scaffolds has been presented in previous papers[37, 50, 51].
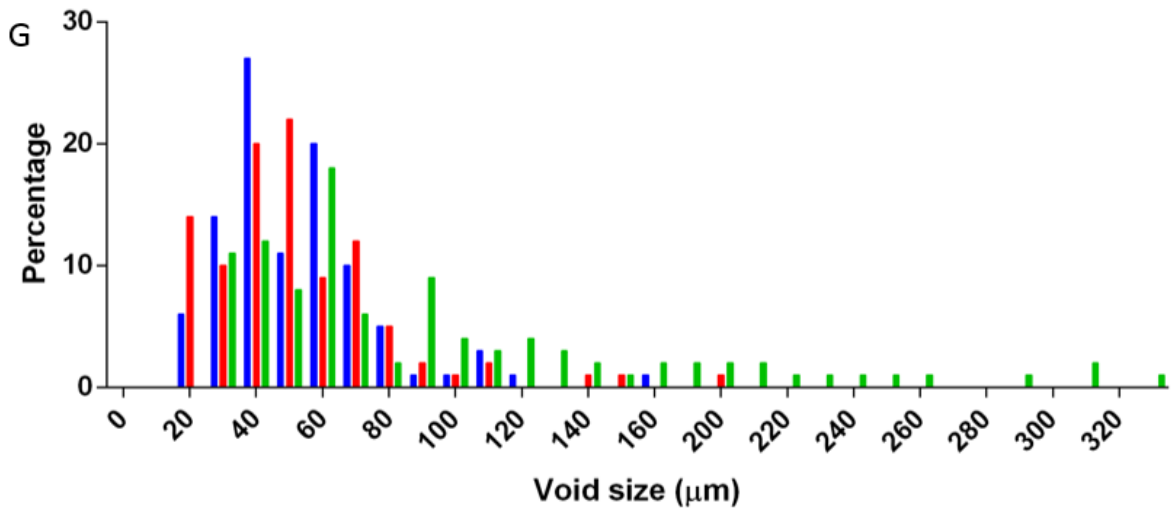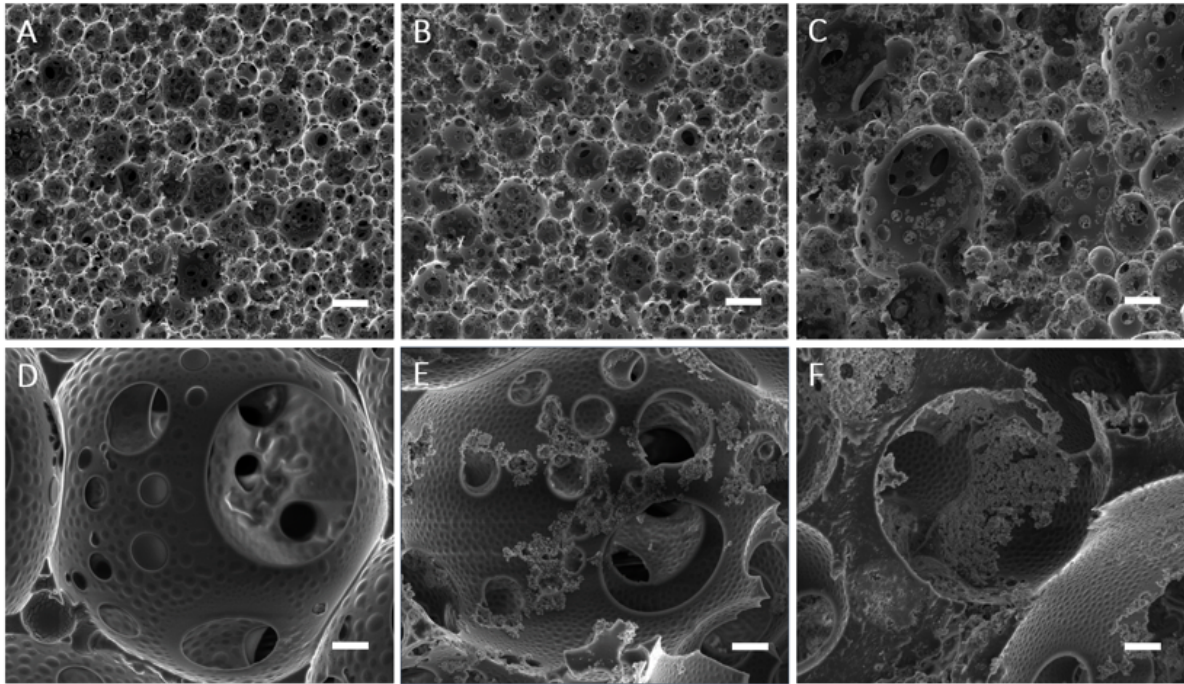
Figure 2. Scanning electron microscope images of scaffolds at 500x (A, B, C) and 5000x (D, E, F) magnification. A,D – PolyHIPE scaffold, B,E – PolyHIPE scaffold + 5 wt% hydroxyapatite, (D,F) – PolyHIPE scaffold + 10 wt% hydroxyapatite. Scale bars represent 100 µm and 10 µm for low and high magnification respectively. G –Void size distribution of polyHIPE scaffold materials based on the percentage of voids with a given diameter. Blue shows the

distribution for the native polyHIPE scaffold, in red is the distribution for the PHP-5HA scaffold and in green is the distribution for the PHP-10HA scaffold.

A key comparator used to evaluate polyHIPE morphology is the average void diameter which was determined by measuring 100 random representative voids and applying a statistical correction factor. A mean void diameter of 58±23 µm was attained for the native polyHIPE structure and a mean void diameter of 57±28 µm was determined for PHP-5HA. The distribution of the void sizes is described in Figure 2 with no substantial differences observable between PHP and PHP-5HA. At 10 wt% hydroxyapatite, the mean void diameter becomes 99±66 µm and significant elongation of the upper tail occurs, indicative of a reduction in HIPE stability.
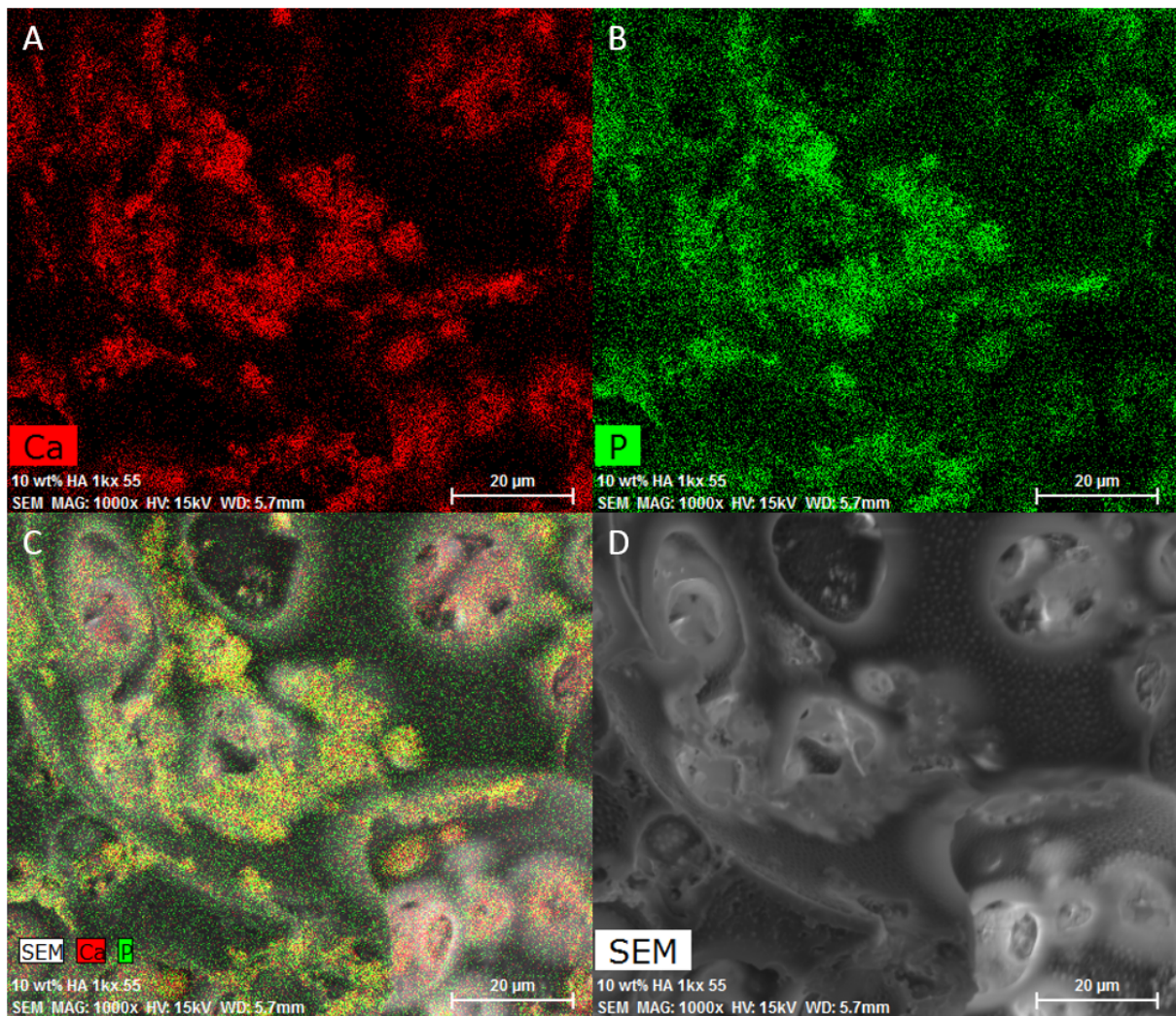
Figure 3. Energy dispersive x-ray spectroscopy elemental mapping of polyHIPE materials containing 10 wt% hydroxyapatite. A – area map highlighting the presence of calcium shown in red, B – area map highlighting the presence of phosphorus shown in green, C – overlay map of calcium and phosphorus, D – SEM image of scanned region.

EDX analysis of the polyHIPE highlights the spread of nanoparticles in the polymer matrix. The high level of concordance between the calcium and phosphate signals suggests

the presence of the added hydroxyapatite. Hydroxyapatite nanoparticles are well dispersed through the matrix with some larger agglomerations.

FTIR Spectroscopy

Incorporation of hydroxyapatite into the polymer scaffold can be shown through FTIR spectroscopy. Hydroxyapatite analysed as-supplied produces a double peak at 569 cm^{-1} and 604 cm^{-1} as well as a strong peak with a shoulder 1030 cm^{-1} which correspond to vibrational modes in the phosphate moiety. The polymer matrix presents with a sharp peak at 1730 cm^{-1} corresponding to the C=O stretch as well as a C-H stretch at 2853 cm^{-1}. In the composite, the peaks from the phosphate group are readily visible as well as the absorptions from the polymer phase. The appearance of these absorbance bands in the phosphate region which do not appear in the native polymer demonstrate the incorporation of hydroxyapatite to form a composite.
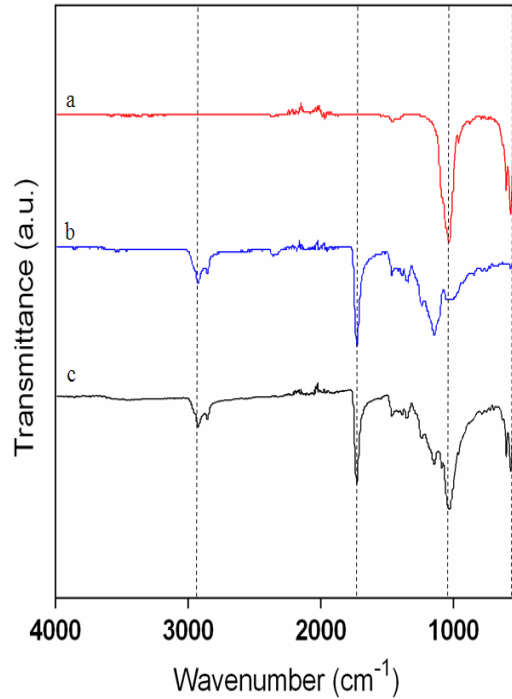
Figure 4. FTIR spectra of the (a) hydroxyapatite nanoparticles, (b) polyHIPE scaffold and (c) polyHIPE + 5 wt% hydroxyapatite composite scaffold

X-ray photoelectron spectroscopy

Compositional analysis of ceramic powders as well as polymer-ceramic composites was carried out using XPS (Table 3). Between PHP-5HA and PHP-10HA, the ratio of oxygen to carbon increased due to the further addition of phosphate. XPS also highlights the incorporation of strontium into hydroxyapatite as evidenced by the comparison between strontium substituted hydroxyapatite powder (SrHA) and hydroxyapatite powder as well as PHP-5SrHA and PHP-5HA. Furthermore, the calcium to phosphate ratio in strontium

substituted hydroxyapatite is reduced as a consequence of the replacement of calcium in the lattice with strontium.

Table 3. XPS results on polyHIPE composite materials (atomic concentrations in %)

Sample[a]	C	O	S	Ca	P	Sr	O/C	Ca/P
HA	13.3	54.7	-	18.7	12.3	-	4.1	1.5
SrHA	14.0	54.4	-	17.7	12.4	1.4	3.9	1.4
PHP-5HA	79.0	17.5	2.3	0.6	0.6	-	0.2	1.1
PHP-5SrHA	83.3	14.6	1.4	0.3	0.3	0.1	0.2	0.8
PHP-10HA	74.3	20.9	3.0	1.0	0.8	-	0.3	1.2

[a] HA: native hydroxyapatite, SrHA: strontium substituted hydroxyapatite

Thermogravimetric analysis of polyHIPE composites

Quantification of ceramic loading into the polymer matrices was performed using thermogravimetric analysis (Figure S2). Polymer-composite samples were subjected to elevated temperatures in order to remove organic content and determine the ceramic composition of the composite. At a loading of 5 wt% hydroxyapatite, the mean mass attributable to the ceramic was 4.6% of the original mass. Increasing the loading to 10wt% hydroxyapatite resulted in a mean attributable mass of 10.4 wt% of the polymer composite. This demonstrates that hydroxyapatite added prior the polymerisation can be incorporated

into a polymer-ceramic composite and that the ceramic component remains after several washing steps.

Table 4. Mass loss of polymer-ceramic composites under thermal degradation

Sample[a]	Mass loss (%)
PHP	100 ± 0.5
PHP-5HA	95.4 ± 2.4
PHP-10HA	89.6 ± 0.7

[a] sample key as for Table 1. Results presented as mean ± standard deviation (N=3).

Compression Testing

Mechanical properties of cellular hydroxyapatite composites were evaluated under uniaxial compression to determine their compressive strength and modulus (Table 5). The compressive strength of PHP-10HA is significantly greater than PHP and PHP-5HA (F =21.40, P < 0.0001).

Table 5. Mechanical properties of hydroxyapatite porous scaffold constructs under compression.

Sample[a]	Number of Samples Tested	Compressive Strength (kPa)	Compressive Modulus (MPa)
PHP	7	148 ± 11	2.58 ± 0.36
PHP-5HA	10	153 ± 20	2.34 ± 0.25
PHP-10HA	6	216 ± 32	2.52 ± 0.32

[a] Sample key as in Table 1. Results processed with 1.25 standard deviation of error.

The effects of the addition of hydroxyapatite are to some extent obfuscated by the high degree of heterogeneity in the scaffold mechanical properties which is reflected in the magnitude of the standard deviation of the sample set. This heterogeneity in part reflects the distribution of void diameters within the porous scaffold which results in uneven load distribution and varies between samples. Larger pore diameters within the scaffold mean that local stresses within the matrix will be greater and can influence the spread of results. Moreover, the method employed for incorporating hydroxyapatite at high concentrations appears to compound these influences by producing a very wide void diameter distribution and a large mean void diameter. Hence, potential mechanical benefits provided by the incorporation of hydroxyapatite are also dependent on the morphology of the porous scaffold.

Cell Culture

Biocompatibility of scaffold constructs was evaluated through *in vitro* culture of MG63 osteosarcoma cells. Scaffolds were sectioned into 200 μm thick slices and seeded with cells. Alvetex® 3D scaffolds were selected as the control environment against the native polyHIPE and composite versions. Alvetex® scaffolds present a porous three-dimensional polystyrene network with an average void size of 30-40 μm and were treated under the same conditions as synthesised materials. Composite polyHIPEs were produced with either 5wt% hydroxyapatite or 5wt% strontium-substituted hydroxyapatite to reduce the impact of large void diameters at higher incorporation concentrations on cell phenotype. Due to oblique cutting of sections, PHP-5SrHA samples appear thicker than other scaffold sections which are approximately 200 μm in height. Distribution of cells and degree of mineralisation over the period was determined through histological techniques (Figure 5).
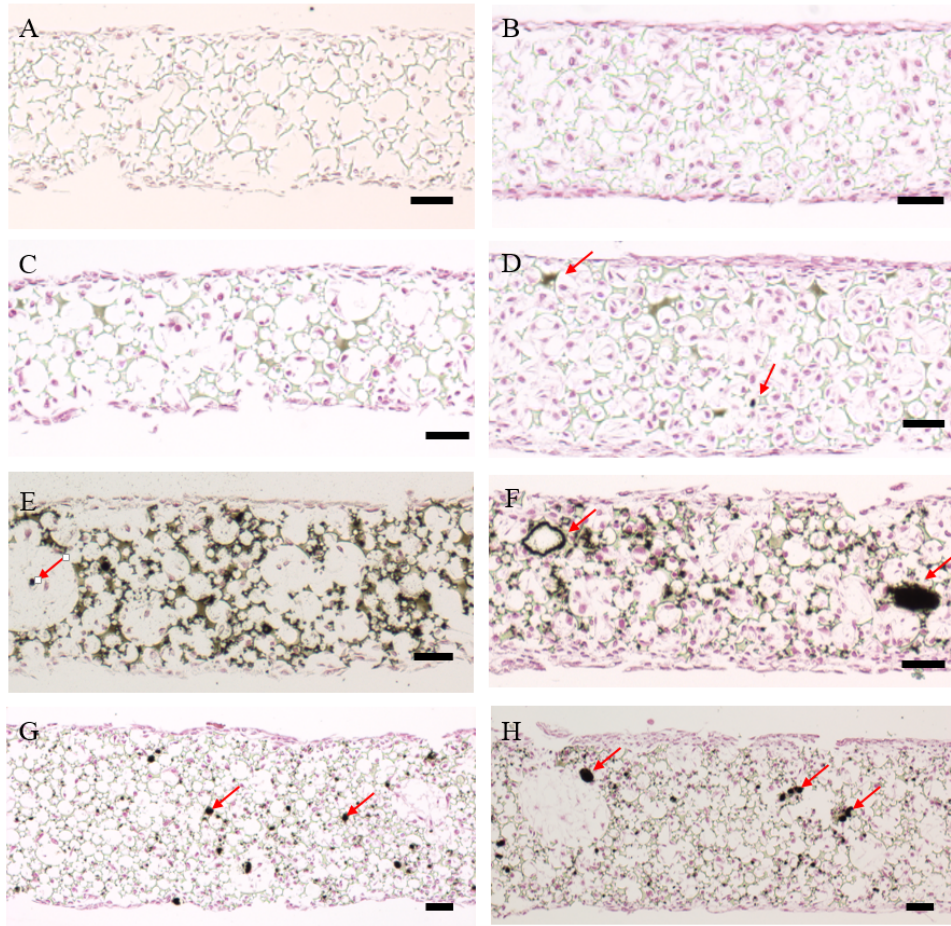
Figure 5. Histologically stained sections of scaffolds cultured for 7 days (A, C, E, G) and 21 days (B, D, F, H); A,B – Alvetex®, C,D – PolyHIPE, E,F – PolyHIPE +5wt% hydroxyapatite, G,H – PolyHIPE + 5wt% strontium-substituted hydroxyapatite. Von Kossa's stain (black colour) was used to indicate the presence hydroxyapatite as well as mineralisation (examples indicated by arrows); cells are counterstained with nuclear fast red. Scale bars represent 100 μm.

Over the culture period, cells were able to migrate through and populate the scaffolds. Cells migrate from the upper open surface to the lower open surface before

dividing and spreading to form a continuous layer and filling the remaining free space within the scaffold. All scaffolds are capable of supporting vigorous growth of MG63 cells. Von Kossa staining, which detects phosphate, was used to investigate mineralization. The extent of von Kossa staining (black colour in Figure 5) is variable across the scaffolds. It should be noted that scaffolds containing HA and SrHA will be positive for von Kossa due to inorganic phosphates present in the hydroxyapatite coating on the scaffold surface. Consequently, ceramic-modified scaffolds at day 7, particularly PHP-5HA, show widespread background staining throughout. Nonetheless, evidence of larger phosphate deposits possibly indicating early onset of mineralization can be seen, most notably in the SrHA sample (arrows in Figure 5E, G). At day 21, the formation of significant quantities of large, von Kossa positive nodules is apparent (Figure 5 F, H), suggesting that mineralisation has progressed further. The nodules on sample PHP-5SrHA are more numerous than those observed in PHP-5HA despite being smaller in size. Furthermore, the background scaffold staining caused by hydroxyapatite is largely absent, indicating dissolution/resorption of HA and SrHA. The scaffolds without HA or SrHA show little evidence of mineralization (Figure 5 B, D)
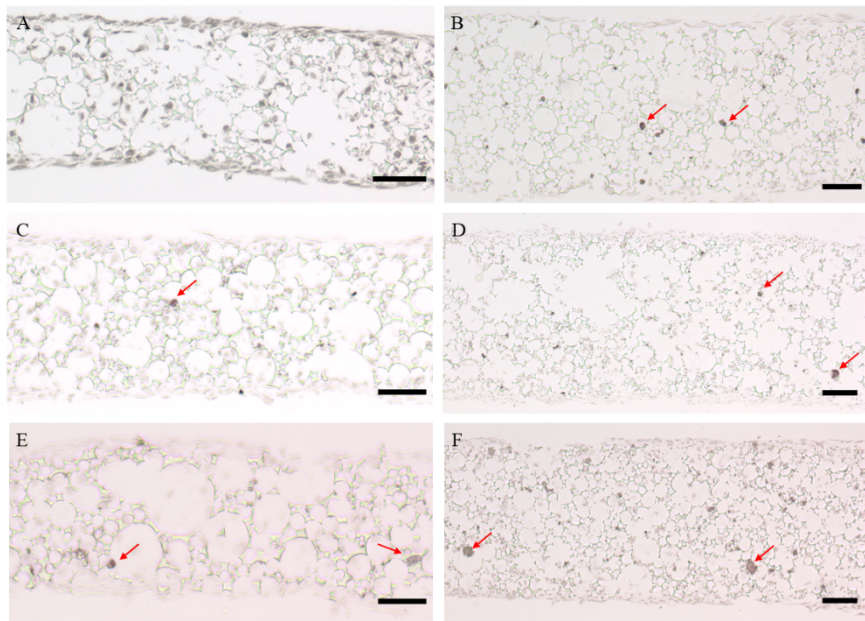
Figure 6. Histologically stained sections of PHP-5HA (A, C, E) and PHP-5SrHA (B, D, F) scaffolds; A,B – Day 7 of culture, C,D – Day 14 of culture, E,F – Day 21 of culture. An Alizarin Red stain was used to indicate the presence hydroxyapatite as well as mineralisation in red (examples indicated by arrows). Scale bars represent 100 μm.

The Alizarin Red (AR) stain was also applied in order to identify the progress of mineralisation within the scaffolds during the culture period (Figure 6). AR staining was used because there is less interference from the scaffold in comparison to von Kossa in terms of stain uptake and it is more sensitive to early time point mineralisation. Furthermore, by implementing both von Kossa and AR staining, calcium and phosphate staining can be compared for overlap to indicate the presence of hydroxyapatite or calcium phosphate. It is evident that over time the number and size of calcium-staining regions increases in both

PHP-5HA and PHP-5SrHA. Strontium-substituted hydroxyapatite appears to have the added benefit of instigating an earlier onset of mineralisation than hydroxyapatite.

Cell adhesion and proliferation on scaffolds was assessed semi-quantitatively by a Bradford total protein assay (Figure 7). Statistically significant differences were observed between Alvetex and PHP-5HA and PHP-5SrHA ($p < 0.01$) at day 7 and at Day 21 ($p < 0.0001$). At day 21, a statistically significant difference was noted between Alvetex and PHP-5HA and PHP-5SrHA and between PHP and PHP-5HA, PHP-5SrHA scaffolds ($p < 0.0001$). Strontium-modified hydroxyapatite and, to a lesser extent, hydroxyapatite both result in a significant increase in cell adhesion and/or proliferation at day 7, compared to Alvetex and unmodified polyHIPE. These results are in agreement with histology data (Figure 5). At later timepoints this trend is replicated, and is particularly evident at day 21 where total protein levels are very much higher on the bioceramic-modified scaffolds compared to those on unmodified scaffolds. Cell adhesion/proliferation is consistently higher on SrHA scaffolds than on those containing HA, in agreement with data on the growth of osteoprecursor cells on HA- and SrHA-coated surfaces[57].
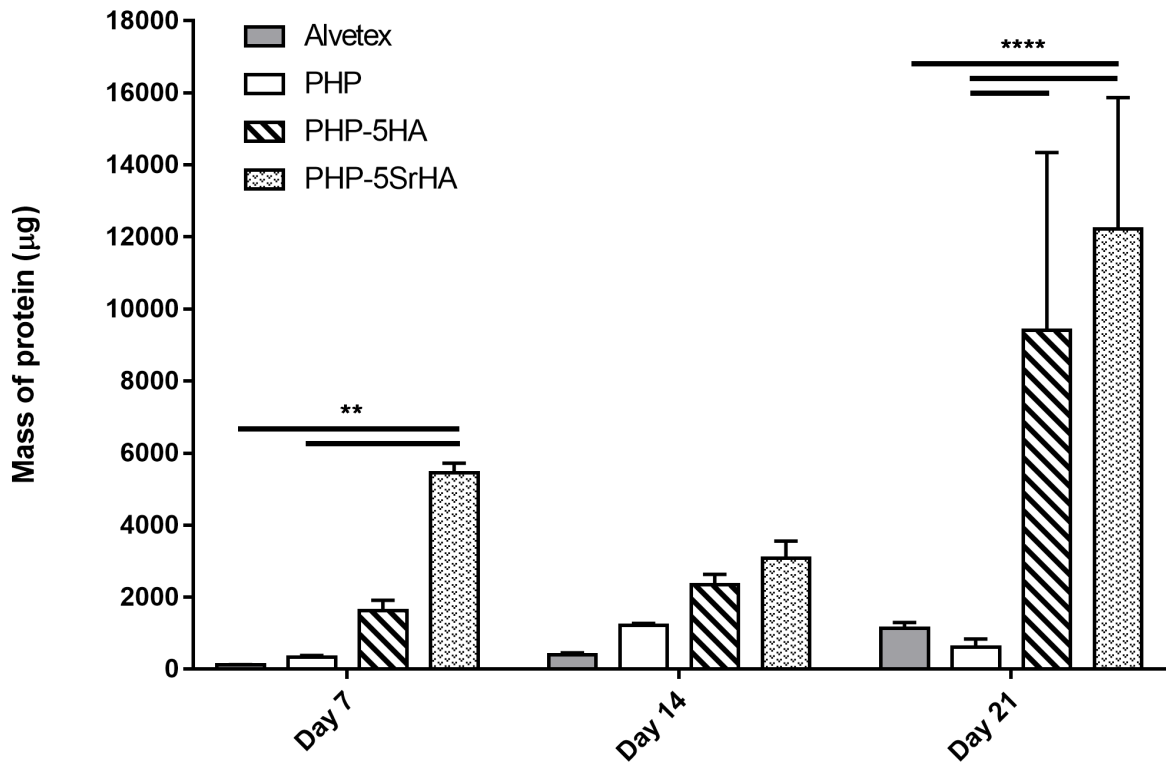
Figure 7. Total protein determination on scaffolds by Bradford assay at day 7, 14 and 21 of culture for each scaffold type presented as mean ± sd (n = 3).

Alkaline phosphatase (ALP) activity of MG63 osteoblastic cells cultured on scaffolds was investigated at days 7, 14 and 21. ALP is an early osteoblastic marker[58], the expression and activity of which has been shown to reduce as cells mature and mineralization begins[59]. Normalized ALP expression (Figure 8) was found to be highest at the earliest timepoint (day 7) for each scaffold type. A statistically significant difference was observed in ALP activity between Alvetex and all other scaffold types (p < 0.0001) at day 7 of culture. Significant

32

differences were also observed between PHP and loaded scaffolds, PHP-5HA and PHP-5SrHA (p < 0.0001 and p < 0.001 respectively). Furthermore, ALP expression at each timepoint was notably higher on unmodified scaffolds compared to those containing HA or SrHA. This suggests a downregulation of ALP and/or loss of ALP activity in the presence of HA or SrHA.
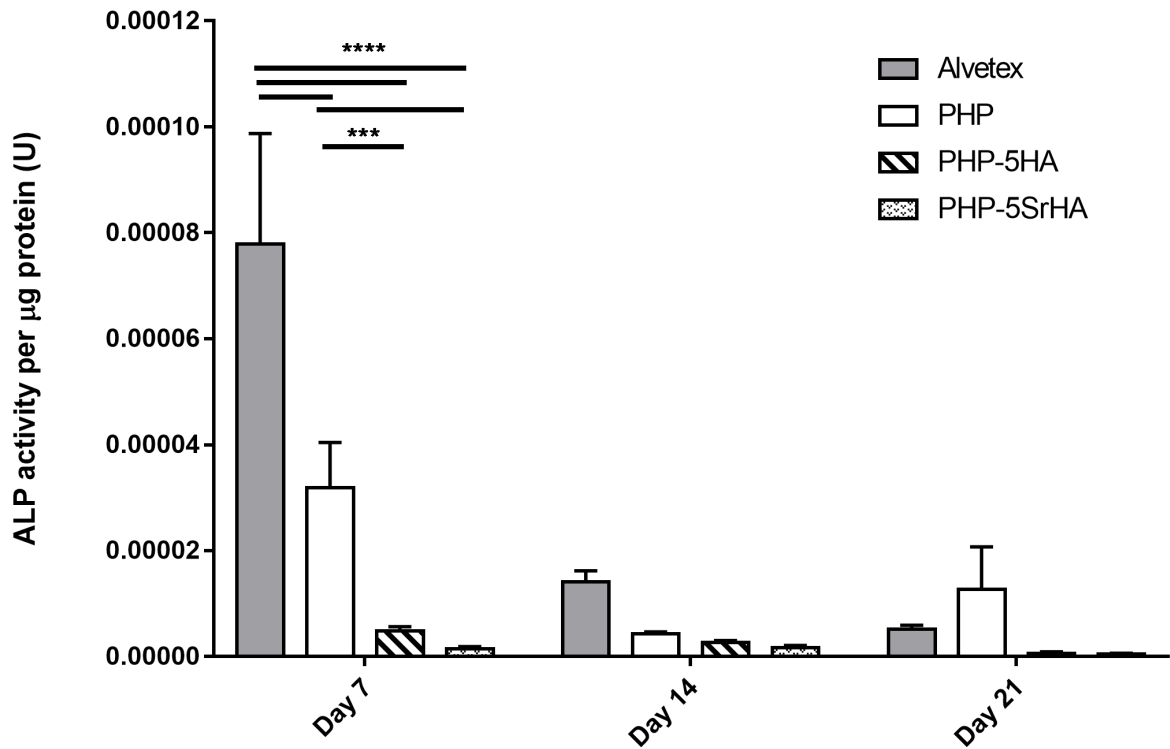

Figure 8. ALP expression per μg of total protein for MG63 cells cultured on scaffolds at day 7, 14 and 21 presented as mean ± sd (n = 3).

Discussion

Porous polymer scaffolds made through the emulsion templating process confer many

advantages such as degradability, surface functionalisation and flexibility in chemistry. In tuning the properties of the emulsion-templated scaffold, a composite approach can be adopted which opens another avenue for tailoring of material properties. Hydroxyapatite is often incorporated into scaffolds used in bone tissue engineering applications as it bears chemical similarity with bone mineral. The chemical composition of the polyHIPE (Figure 1) was based on a highly crosslinked acrylate-thiol system previously described with a tensile Young's modulus of 19MPa[37]. The relatively high modulus of this material lent itself towards bone tissue engineering and was further adapted with the incorporation of hydroxyapatite. Furthermore, strontium has been increasingly recognised as a potent adjuvant to influence bone formation with and without hydroxyapatite and has been linked with promotion of osteoblast activity while inhibiting osteoclasts.

Strontium ions were substituted for calcium in the hydroxyapatite lattice structure through a sorption and ion exchange process. Based on the ICP-OES analysis, a reduction in the strontium concentration in solution was accompanied by an increase in the calcium concentration of the supernatant. Given that the lattice structure simultaneously underwent a minor expansion, strontium is not merely adsorbed on the surface of particles, but has been integrated into the crystal structure of the hydroxyapatite. The minor lattice expansion reflects the larger size of the strontium ion compared to calcium. Furthermore, apart from hydroxyapatite and trace calcium phosphate, no other crystalline phases were identified, suggesting that no new crystalline phases have formed indicating incorporation of strontium by calcium substitution. This is supported by XPS of the supplied

hydroxyapatite in comparison with strontium substituted hydroxyapatite. The atomic concentration of calcium is observed to decrease slightly in the SrHA sample. Notably, when the sum of the atomic concentration of calcium and strontium is divided by the concentration of phosphate a Ca/P ratio is obtained which is equal to the Ca/P ratio of the supplied hydroxyapatite. By substituting strontium into the hydroxyapatite crystal structure, the benefits of hydroxyapatite are preserved while simultaneously providing trace amounts of strontium to aid in mineralisation.

Scaffolds were produced by emulsion templating monomer solutions containing varying ceramic content. At low ceramic concentrations (<5 wt%), there is negligible impact on the overall morphology and distribution of voids. However, at higher concentrations there is a visible destabilising effect on the emulsion as at 10 wt% concentration very large voids are produced. Emulsion destabilisation broadens the pore distribution by introducing a greater number of large voids (>100 μm). Further increases in hydroxyapatite concentration may be of use in facilitating larger void diameters desired in *in vivo* scaffold implants while also providing more hydroxyapatite. Hydroxyapatite is well represented on the surface of the scaffold interior as indicated by the rough texturing observable under SEM. There is a fine and even distribution of nanoparticles through the matrix as well as larger agglomerations which are stable through the washing process.

Analysis of fabricated scaffolds by FTIR showed the presence of sharp phosphate absorbance bands indicative of hydroxyapatite. In particular, the appearance of the double peak at 569 cm^{-1} and 604 cm^{-1} strongly correlates with native hydroxyapatite. Calcium,

phosphate and strontium are detectable in composite scaffolds subjected to XPS. Compared with the ceramic powders, the Ca/P ratio is reduced which implies partial loss of calcium. As the concentration of hydroxyapatite is increased, the O/C ratio also increases due to the presence of phosphate. To confirm the loading of hydroxyapatite into the scaffolds, thermogravimetric analysis in a nitrogen environment was performed. With good agreement between the loaded amount and the mass remaining after burn-off, scaffolds are capable of retaining varying degrees of ceramic.

Mechanical responses of composite scaffolds were determined through uniaxial compression testing. No significant differences were observed in data when an allowable error of 2.8 standard deviations of the mean was applied. To reduce the impact of outlier samples, an allowable error of 1.25 standard deviations was chosen. The compressive strength of PHP-10HA was found to be significantly greater than PHP and PHP-5HA (F=21.40, P < 0.0001). This demonstrates that mean compressive strength of the composites increases with hydroxyapatite loading, while modulus is largely unaffected.

Of particular interest in the design of scaffolds for *in situ* tissue engineering is the matching of the mechanical properties of the scaffold to that of the native tissue as it can have impacts on the local phenotypic response as well as integration and stability. Polymeric bone tissue engineering scaffolds typically suffer from insufficient mechanical strength while ceramic and metal scaffolds exhibit much higher strength. To more closely mimic native bone which has inherent flexibility and strength, composite materials can address the shortcomings of pure materials. This is further complicated by the variation observed in

bone as well as the complex loading conditions. Our material has been designed considering use as a defect filler and support for additional therapy in the context of trabecular mandibular bone. The Young's modulus of [human] mandibular bone has been reported by Misch *et al.* as being between 3.5-125.6 MPa. Given a compression modulus of approximately 2.4 MPa determined for dry polyHIPE scaffolds, mechanical properties are approaching the lower end of native tissue. Previous studies indicated a tensile Young's modulus of 19 MPa for this material[37]. Principally, this discrepancy arises from the size difference between compression and tensile samples and the lower strain that was applied in compression compared to tension. At present, hydroxyapatite is incorporated by polymerising the network around particles and the level of interaction is limited. This has implications for the degree of strengthening which can be attained and there is scope for improving the transference of load between the polymer and the ceramic phase.

No significant adverse effects were observed during culture of MG63 cells on any of the polyHIPE scaffolds compared to Alvetex® cultures. Cell penetration into the scaffolds remained high across all samples with colonisation sustained throughout the scaffold over the culture period. Preliminary results indicate that the incorporation of hydroxyapatite and strontium-modified hydroxyapatite into the scaffold both enhances mineralisation and promotes an earlier onset of mineralisation. Furthermore, the incorporation of Sr appears to enhance mineralization across all timepoints. As limited mineralisation has occurred in samples without added ceramic, the observed changes are likely to occur through redistribution of hydroxyapatite, indicating its bioavailability.

The presence of strontium appears to enhance osteoblastic cell proliferation. Strontium-modified hydroxyapatite was shown to result in a more rapid formation of a surface apatite layer in simulated body fluid experiments than hydroxyapatite, indicating enhanced bioactivity[57]. Replacement of some of the Ca by Sr influences hydroxyapatite dissolution behaviour. The same study also showed enhanced osteoprecursor cell adhesion on SrHA surfaces compared to HA, promoted an osteoblastic phenotype and significantly increased cell proliferation.

ALP expression is highest on scaffolds without added hydroxyapatites, and in most cases diminishes as time progresses. It is known that ALP is down-regulated once mineralization is established[59]. Polak et al. observed a large reduction in levels of ALP activity between days 2 and 12 of osteoblast culture on bioactive glass[60]. At the same time, calcified bone nodule formation was observed on bioglass surfaces as early as day 6. Rat osteoblasts[61] cultured in the presence of calcium phosphate bioceramics, including HA, displayed a rapid drop in ALP expression levels after day 3. Addition of soluble calcium to 3D cultures of MG63 cells has similarly been shown to enhance mineralization and, to a lesser extent, down-regulate ALP expression[62]. We hypothesise therefore that the presence of HA or SrHA encourages early mineralization of scaffolds, which in turn results in a down-regulation of ALP, in comparison to scaffolds without added bioceramic. This explains the observed formation of calcium- and phosphate-rich nodules as well as the significantly lower levels of ALP expression at day 7 in the presence of HA and SrHA, compared to control scaffolds.

While the current approach taken is unable to quantify the contributions to the microenvironment which trigger mineralisation events in these scaffolds, strontium-substitution into hydroxyapatite appears to result in more reliable and earlier formation of bone nodules. Hydroxyapatite by itself can produce larger regions of mineralisation even if the occurrence is rarer. Further investigation into the osteogenic gene expression profiles may better elucidate and quantify the difference between hydroxyapatite and strontium-substituted hydroxyapatite in these scaffolds. Primary evaluation of the scaffold materials has been accomplished using thin scaffold sections of approximately 200μm thick which limits the maximum diffusion distance to cells. For translation to an *in vivo* context, sufficient vascularisation will be required to support growth into the scaffold as well as host integration. As such, controllable enlargement of internal voids coupled with strength compensation remains the crux for future scaffold development.

Conclusions

It has been demonstrated that thiol-acrylate polyHIPEs can be fabricated as nanocomposites containing ceramic nanoparticle inclusions. The content of the formulation can have significant effects on the morphology of the scaffold formed with a relatively high particle loading negatively affecting the stability of the emulsion. MG63 cells cultured on the bioceramic composite scaffolds showed improved mineralisation compared with those cultured on polymer-only scaffolds which highlights the bioavailability of hydroxyapatite to the culture. Furthermore, cell proliferation was enhanced on composite scaffolds, in

particular those containing Sr. High cell densities maintained over the extended culture period are evidence that the scaffolds are biocompatible. Further work to tailor the scaffold to better support osteogenesis as well as *in vivo* evaluation will be needed to progress towards *in situ* bone tissue engineering for defect repair.

Acknowledgements

References

1.   A. R. Amini, C. T. Laurencin and S. P. Nukavarapu, *Crit. Rev. Biomed. Eng.*, 2012, **40**, 363-408.

2.   H.-S. Roh, S.-C. Jung, M.-S. Kook and B.-H. Kim, *Appl. Surf. Sci.*, 2016, **388, Part A**, 321-330.

3.   S. Taherkhani and F. Moztarzadeh, *J. Appl. Polym. Sci.*, 2016, **133**.

4.   E. Tayton, M. Purcell, A. Aarvold, J. O. Smith, S. Kalra, A. Briscoe, K. Shakesheff, S. M.

Howdle, D. G. Dunlop and R. O. Oreffo, *Acta Biomater.*, 2012, **8**, 1918-1927.

5. Y. Zhang, J. R. Venugopal, A. El-Turki, S. Ramakrishna, B. Su and C. T. Lim, *Biomaterials*, 2008, **29**, 4314-4322.

6. N. R. Cameron, *Polymer*, 2005, **46**, 1439-1449.

7. N. R. Cameron, P. Krajnc and M. S. Silverstein, in *Porous Polymers*, eds. M. S. Silverstein, N. R. Cameron and M. A. Hillmyer, Wiley & Sons, Hoboken, N.J., 2011, pp. 119-172.

8. R. J. Carnachan, M. Bokhari, S. A. Przyborski and N. R. Cameron, *Soft Matter*, 2006, **2**, 608-616.

9. S. D. Kimmins and N. R. Cameron, *Adv. Funct. Mater.*, 2011, **21**, 211-225.

10. I. Pulko and P. Krajnc, *Macromol. Rapid Commun.*, 2012, **33**, 1731-1746.

11. M. S. Silverstein, *Prog. Polym. Sci.*, 2014, **39**, 199-234.

12. M. S. Silverstein, *Polymer*, 2014, **55**, 304-320.

13. D. Barby and Z. Haq, *EP Pat.,* 60138, 1982.

14. J. M. Williams, *Langmuir*, 1988, **4**, 44-49.

15. H. F. Zhang and A. I. Cooper, *Soft Matter*, 2005, **1**, 107-113.

16. E. Ruckenstein, *Adv. Polym. Sci.*, 1997, **127**, 1-58.

17. K. Haibach, A. Menner, R. Powell and A. Bismarck, *Polymer*, 2006, **47**, 4513-4519.

18. K. J. Lissant (ed.), *Emulsions and Emulsion Technology Part 1*, Marcel Dekker Inc., New York, 1974.

19. G. Akay, Z. Bhumgara and R. J. Wakeman, *Chem. Eng. Res. Des.*, 1995, **73**, 782-797.

20. P. Krajnc, N. Leber, J. F. Brown and N. R. Cameron, *React. Funct. Polym.*, 2006, **66**, 81-91.

21. G. H. Ruan, Z. W. Wu, Y. P. Huang, M. P. Wei, R. H. Su and F. Y. Du, *Biochem. Biophys. Res. Commun.*, 2016, **473**, 54-60.

22. R. H. Su, G. H. Ruan, H. G. Nie, T. Xie, Y. J. Zheng, F. Y. Du and J. P. Li, *J. Chromatogr. A*, 2015, **1405**, 23-31.

23. P. W. Small and D. C. Sherrington, *J. Chem. Soc., Chem. Commun.*, 1989, 1589-1591.

24. H. Deleuze, B. Maillard and O. Mondain-Monval, *Bioorg. Med. Chem. Lett.*, 2002, **12**, 1877-1880.

25. S. Hus, M. Kolar and P. Krajnc, *J. Chromatogr. A*, 2016, **1437**, 168-175.

26. S. Kovacic, M. Mazaj, M. Jeselnik, D. Pahovnik, E. Zagar, C. Slugovc and N. Z. Logar, *Macromol. Rapid Commun.*, 2015, **36**, 1605-1611.

27. G. Akay, M. Birch and M. Bokhari, *Biomaterials*, 2004, **25**, 3991-4000.

28. M. W. Hayman, K. H. Smith, N. R. Cameron and S. A. Przyborski, *Biochem. Biophys. Res. Commun.*, 2004, **314**, 483-488.

29. M. A. Bokhari, G. Akay, S. Zhang and M. A. Birch, *Biomaterials*, 2005, **26**, 5198-5208.

30. M. W. Hayman, K. H. Smith, N. R. Cameron and S. A. Przyborski, *J. Biochem. Biophys. Methods*, 2005, **62**, 231-240.

31. M. Bokhari, R. J. Carnachan, N. R. Cameron and S. A. Przyborski, *Biochem. Biophys. Res. Commun.*, 2007, **354**, 1095-1100.

32. M. Bokhari, R. J. Carnachan, N. R. Cameron and S. A. Przyborski, *J. Anat.*, 2007, **211**,

567-576.

33.   M. Bokhari, R. J. Carnachan, S. A. Przyborski and N. R. Cameron, *J. Mater. Chem.*, 2007, **17**, 4088-4094.

34.   E. M. Christenson, W. Soofi, J. L. Holm, N. R. Cameron and A. G. Mikos, *Biomacromolecules*, 2007, **8**, 3806-3814.

35.   E. Knight, B. Murray, R. Carnachan and S. Przyborski, in *3D Cell Culture: Methods and Protocols*, 2011, vol. 695, pp. 323-340.

36.   R. S. Moglia, J. L. Holm, N. A. Sears, C. J. Wilson, D. M. Harrison and E. Cosgriff-Hernandez, *Biomacromolecules*, 2011, **12**, 3621-3628.

37.   S. Caldwell, D. W. Johnson, M. P. Didsbury, B. A. Murray, J. J. Wu, S. A. Przyborski and N. R. Cameron, *Soft Matter*, 2012, **8**, 10344-10351.

38.   A. S. Hayward, A. M. Eissa, D. J. Maltman, N. Sano, S. A. Przyborski and N. R. Cameron, *Biomacromolecules*, 2013, **14**, 4271-4277.

39.   A. S. Hayward, N. Sano, S. A. Przyborski and N. R. Cameron, *Macromol. Rapid Commun.*, 2013, **34**, 1844-1849.

40.   S. Zhou, A. Bismarck and J. H. G. Steinke, *J. Mater. Chem. B*, 2013, **1**, 4736-4745.

41.   R. Owen, C. Sherborne, G. C. Reilly and F. Claeyssens, *Data Brief*, 2015, **5**, 616-620.

42.   M. Susec, R. Liska, G. Russmuller, J. Kotek and P. Krajnc, *Macromol. Biosci.*, 2015, **15**, 253-261.

43.   J. Naranda, M. Susec, U. Maver, L. Gradisnik, M. Gorenjak, A. Vukasovic, A. Ivkovic, M. S. Rupnik, M. Vogrin and P. Krajnc, *Sci. Rep.*, 2016, **6**.

44. R. Owen, C. Sherborne, T. Paterson, N. H. Green, G. C. Reilly and F. Claeyssens, *J. Mech. Behav. Biomed. Mater.*, 2016, **54**, 159-172.

45. J. L. Robinson, M. A. P. McEnery, H. Pearce, M. E. Whitely, D. J. Munoz-Pinto, M. S. Hahn, H. Li, N. A. Sears and E. Cosgriff-Hernandez, *Tiss. Eng. Pt. A*, 2016, **22**, 403-414.

46. A. Barbetta, M. Massimi, L. C. Devirgiliis and M. Dentini, *Biomacromolecules*, 2006, **7**, 3059-3068.

47. A. Barbetta, M. Massimi, B. Di Rosario, S. Nardecchia, M. De Colli, L. C. Devirgiliis and M. Dentini, *Biomacromolecules*, 2008, **9**, 2844-2856.

48. M. De Colli, M. Massimi, A. Barbetta, B. L. Di Rosario, S. Nardecchia, L. C. Devirgiliis and M. Dentini, *Biomed. Mater.*, 2012, **7**, 055005.

49. J. L. Robinson, R. S. Moglia, M. C. Stuebben, M. A. P. McEnery and E. Cosgriff-Hernandez, *Tiss. Eng. Pt. A*, 2014, **20**, 1103-1112.

50. E. Lovelady, S. D. Kimmins, J. Wu and N. R. Cameron, *Polym. Chem.*, 2011, **2**, 559-562.

51. D. W. Johnson, C. R. Langford, M. P. Didsbury, B. Lipp, S. A. Przyborski and N. R. Cameron, *Polym. Chem.*, 2015, **6**, 7256-7263.

52. C. R. Langford, D. W. Johnson and N. R. Cameron, *Macromol. Rapid Commun.*, 2015, **36**, 834-839.

53. B. Fernández-Montes Moraleda, S. Román and L. M. Rodríguez-Lorenzo, *J. Biomed. Mater. Res. Pt. A*, 2016.

54. L. M. Rodriguez-Lorenzo, in *Apatite: Synthesis, Structural Characterization and*

Biomedical Applications, eds. M. Iafisco and J. M. Delgado Lopez, NOVA Publishers, Hauppage, NY, 2014.

55.   A. Barbetta and N. R. Cameron, *Macromolecules*, 2004, **37**, 3202-3213.

56.   A. Barbetta and N. R. Cameron, *Macromolecules*, 2004, **37**, 3188-3201.

57.   W. C. Xue, J. L. Moore, H. L. Hosick, S. Bose, A. Bandyopadhyay, W. W. Lu, K. M. C. Cheung and K. D. K. Luk, *J. Biomed. Mater. Res. Pt. A*, 2006, **79A**, 804-814.

58.   J. E. Aubin, in *Principles of Bone Biology (Third Edition)*, eds. J. P. Bilezikian, L. G. Raisz and T. J. Martin, Academic Press, Cambridge, MA, 2008, vol. 1.

59.   T. A. Owen, M. Aronow, V. Shalhoub, L. M. Barone, L. Wilming, M. S. Tassinari, M. B. Kennedy, S. Pockwinse, J. B. Lian and G. S. Stein, *J. Cell. Physiol.*, 1990, **143**, 420-430.

60.   I. D. Xynos, M. V. J. Hukkanen, J. J. Batten, L. D. Buttery, L. L. Hench and J. M. Polak, *Calcified Tissue Int.*, 2000, **67**, 321-329.

61.   J. S. Sun, Y. H. Tsuang, C. J. Liao, H. C. Liu, Y. S. Hang and F. H. Lin, *J. Biomed. Mater. Res.*, 1997, **37**, 324-334.

62.   Y. Takagishi, T. Kawakami, Y. Hara, M. Shinkai, T. Takezawa and T. Nagamune, *Tiss. Eng.*, 2006, **12**, 927-937.